REPORT DOCUMENTATION PAGE

Form Approved
OMB No. 0704-0188

1. REPORT DATE *(DD-MM-YYYY)*	2. REPORT TYPE	3. DATES COVERED *(From - To)*
03-11-2006	FINAL	01/01/2003 – 12/31/2005

4. TITLE AND SUBTITLE
Shock Control and Power Extraction by MHD Processes in Hypersonic Air Flow

5a. CONTRACT NUMBER

5b. GRANT NUMBER
F49620-03-1-0028

5c. PROGRAM ELEMENT NUMBER

6. AUTHOR(S)

Prof. Richard B. Miles and Dr. Sergey O. Macheret

5d. PROJECT NUMBER

5e. TASK NUMBER

5f. WORK UNIT NUMBER

7. PERFORMING ORGANIZATION NAME(S) AND ADDRESS(ES)

Princeton University
Dept. Mechanical & Aerospace Engineering
Olden Street
Princeton, NJ 08544

8. PERFORMING ORGANIZATION REPORT NUMBER

9. SPONSORING / MONITORING AGENCY NAME(S) AND ADDRESS(ES)
Air Force Office of Scientific Research
875 North Randolph St.
Arlington, VA 22203
Dr John Schmisseur/NA

10. SPONSOR/MONITOR'S ACRONYM(S)
AFOSR

11. SPONSOR/MONITOR'S REPORT NUMBER(S)

12. DISTRIBUTION / AVAILABILITY STATEMENT

Approved for public release; distribution is unlimited

AFRL-SR-AR-TR-06-0457

13. SUPPLEMENTARY NOTES

14. ABSTRACT
This project was a theoretical and experimental research effort on the use of MHD body forces and plasmas for boundary layer control and power extraction in supersonic flow, and on the development of new diagnostics for plasmas and for high-speed flows. The first part of this final report addresses MHD processes for control and power extraction. This section includes the constricted DC driven "snowplow arc" discharge that can potentially be used to accelerate the boundary layer for suppression of separation, volumetric MHD for power extraction, and volumetric MHD for flow control. In order to accomplish volumetric MHD in cold air, a high repetition rate, short pulse sustainer concept is developed and applied for the first demonstration of power extraction from cold supersonic air. The following section addresses non MHD plasma methods of flow control and power extraction, particularly through the use of a dielectric barrier discharge and through a new pulse sustained thermionic power generator embedded into the hot walls of the vehicle engine. Finally, two new diagnostic methods are introduced in the third section: magnetically modulated microwave attenuation for the measurement of electron number density and electron collision frequency, and Radar REMPI for the localized measurement of flow velocity.

15. SUBJECT TERMS
Diagnostic methods, MHD, Boundary layer control, high-speed flows, plasmas

16. SECURITY CLASSIFICATION OF:			17. LIMITATION OF ABSTRACT	18. NUMBER OF PAGES	19a. NAME OF RESPONSIBLE PERSON
Unclassified					Prof. Richard B. Miles
a. REPORT	b. ABSTRACT	c. THIS PAGE	UL	30	19b. TELEPHONE NUMBER *(include area code)*
Unclassified	Unclassified	Unclassified			609-258-5131

Standard Form 298 (Rev. 8-98)
Prescribed by ANSI Std. Z39.18

Shock Control and Power Extraction by MHD Processes in Hypersonic Air Flow

AFOSR GRANT #FA49620-03-1-0028

Richard B. Miles and Sergey O. Macheret
Department of Mechanical & Aerospace Engineering
Princeton University, Princeton, NJ

Final Report

Abstract

This project was a theoretical and experimental research effort on the use of MHD body forces and plasmas for boundary layer control and power extraction in supersonic flow, and on the development of new diagnostics for plasmas and for high-speed flows. The first part of this final report addresses MHD processes for control and power extraction. This section includes the constricted DC driven "snowplow arc" discharge that can potentially be used to accelerate the boundary layer for suppression of separation, volumetric MHD for power extraction, and volumetric MHD for flow control. In order to accomplish volumetric MHD in cold air, a high repetition rate, short pulse sustainer concept is developed and applied for the first demonstration of power extraction from cold supersonic air. The following section addresses non MHD plasma methods of flow control and power extraction, particularly through the use of a dielectric barrier discharge and through a new pulse sustained thermionic power generator embedded into the hot walls of the vehicle engine. Finally, two new diagnostic methods are introduced in the third section: magnetically modulated microwave attenuation for the measurement of electron number density and electron collision frequency, and Radar REMPI for the localized measurement of flow velocity.

I. MHD PROCESSES AND VOLUMETRIC IONIZATION

A. Studies of High Repetition Rate Magnetically Accelerated Snowplow Arcs, and Their Effects on Shock-Boundary Layer Interactions and Flow Separation

Our measurements indicate that nonequilibrium ("cold") surface arcs can be magnetically driven both downstream and upstream (depending on the B field direction) at a velocity of up to 5-7 kilometers/second. If those arcs can couple well to the flow, they may have the potential of accelerating the boundary layer and controlling separation. The surface arc is struck between two slightly diverging linear electrodes that are attached to the surface and oriented in the direction of the flow (Fig. 1). When a high voltage is applied between the electrodes, a confined discharge or arc forms at the point of smallest separation. The arc is then convected with the flow and blows out downstream where the electrodes end. At that instant another arc is formed at the upstream point, and the process repeats. Because of the high speed of the flow, the discharge appears uniform to the eye (Fig. 2), but when imaged with a fast camera, one arc is clearly seen (those images are not shown in Fig. 2). By changing the exposure time on the camera, the blurring of the arc can be used to determine its velocity. The left side of Figure 2 shows images of the 35 mA, 1.2-1.8 kV arc taken at 1, 10 and 50 microsecond exposures, indicating that the arc

speed is 425 m/s. That corresponds to a location at about 10% of the boundary layer thickness for this flow of 600 m/s. On the right side of Figure 2 the arc motion with a magnetic field of 2 T applied perpendicular to the surface is shown. The magnetic field accelerates the arc and cants it somewhat because of the Hall effect. The arc now moves at 5,000-7,000 m/s as measured by the exposure time of the camera. The intention is to use this increased speed to force the boundary layer flow so that the boundary layer is accelerated. If this can be accomplished, then the arc may be used for the suppression of boundary layer separation in supersonic flows.

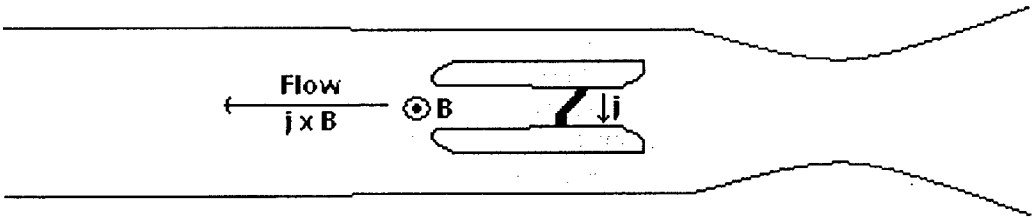

Figure 1. Sidewall electrodes in the test section of Mach 3 tunnel for studies of snowplow arcs. The magnetic field is perpendicular to the plane of the figure.

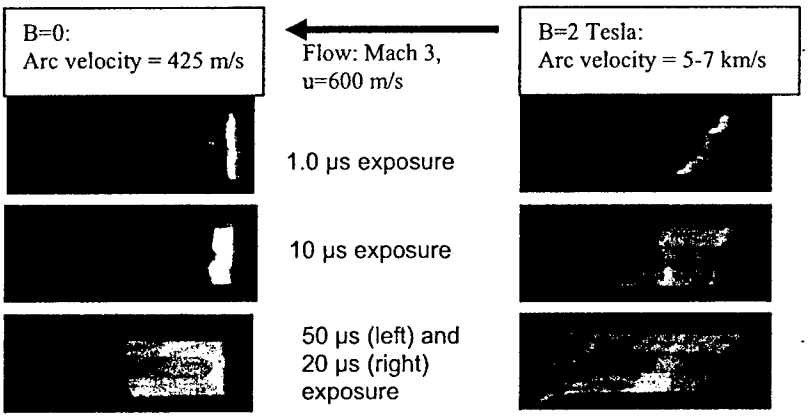

Figure 2. 35-milliampere surface arc in the Mach 3 flow at different exposures without magnetic field (left) or accelerated by a 2 Tesla magnetic field (right). Flow is from right to left. Measurement of the arc displacement over these times gives a speed of magnetically accelerated arc of between 5,000 and 7,000 m/s.

The performance of the snowplow arc is limited by the heating of the electrodes. A collaboration with CMI, Inc. has led to the development of a new sapphire-based, electrode/dielectric element shown in Fig. 3 (bottom inset). This utilizes a titanium copper electrode that is thermally matched to the sapphire, so the unit is robust to heating. Because of the high thermal conductivity of the sapphire it is expected that this will permit higher current densities, and, thus, more efficient coupling to the boundary layer. The device is mounted into a transparent in-draft wind tunnel and inserted into our superconducting magnet. The wind tunnel is currently being

instrumented with pressure taps and fitted with a shock generating wedge on the opposite side so the effects of the snow plow arc on shock-induced separation can be observed.

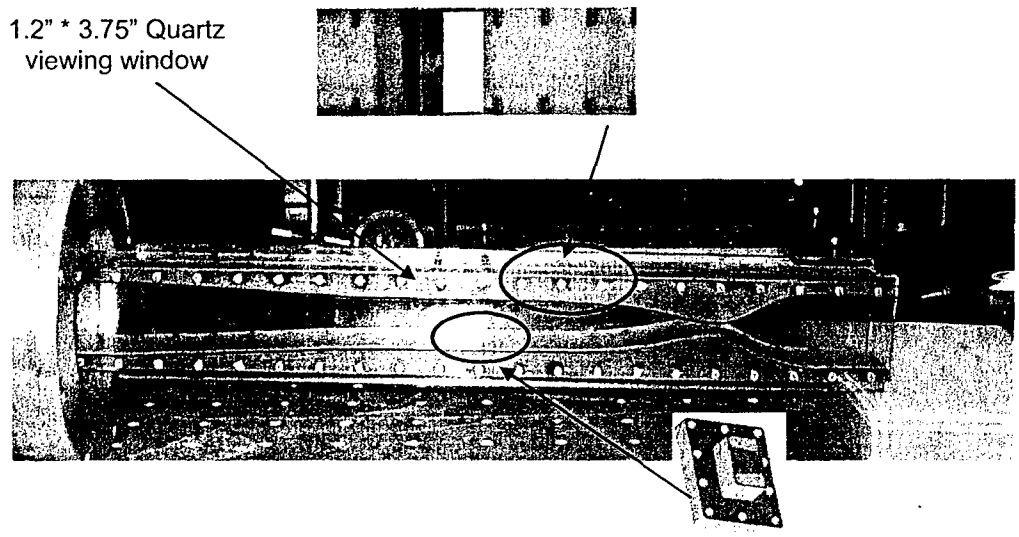

Figure 3: Mach 2.4 in-draft wind tunnel with the test section showing the electrodes and a 10 degree wedge to create a shockwave. The sapphire insert with embedded electrodes is shown in the lower inset.

Theoretical analysis shows that the electron and ion densities in the weakly ionized arc are about $n_e \approx 2.5\times10^{11}$ cm^{-3}, corresponding to the ionization fraction of $n_e/n \approx 2.5\times10^{-7}$. The electron and ion Hall parameters at B=2 T are: $\Omega_e \approx 3\text{-}4.2$, $\Omega_i \approx (1.4\text{-}2)\times10^{-2}$, and the ion slip parameter $\Omega_e\Omega_i \approx (4.3\text{-}8.4)\times10^{-2}$. The physics of snowplow arc motion is the following:

> The electrons experience the Lorentz force that tries to pull them away from ions. The Lorentz force experienced by ions is quite small, but the slight polarization of the plasma creates an electric field that slows the electrons and "glues" them to the ions. Thus, electrons and ions move together. The ions then couple to the neutral gas.

Calculations show that the gas velocity increment in a single sweep of the arc is quite small, less than 1 m/s. However, as the gas element in the boundary layer slowly moves along the wall, it experiences many "hits" by the consecutive arcs, and the resulting velocity increment is about 15-30 m/s. Preliminary measurements indicate that the Mach number at the wall increases with the magnetic field, suggesting that flow acceleration may indeed be happening. Estimates also show that the heating caused by the running arc can also be significant, at least on the order 30-50 K.

Further theoretical work has sought to develop a more thorough understanding of the push work and heat generation, as well as to understand the observed physical attributes of the arc, with the intention of optimizing its potential for boundary layer flow control. In this case, minimization of heating versus push work is the paramount issue. Theoretical analysis shows that the heating can be considerably reduced by operating in a regime dramatically different from that in the

early experiments. Equation 1 shows the ratio of the push work to the Joule heat dissipation, where $\mu_{e,i}$ is the average gas velocity of the boundary layer (Eq. 2), E and B are the electric and magnetic field strengths, and Ω_e and Ω_i are the electron and ion Hall parameters.

$$\frac{\text{push work}}{\text{Joule dissipation}} = \frac{u_{e,i}B}{E - u_{e,i}B} \qquad \textbf{(Eq 1)}$$

$$u_{e,i} = \frac{u + (E/B)\Omega_e\Omega_i}{1 + \Omega_e\Omega_i} \qquad \textbf{(Eq 2)}$$

If the applied electric field is made very weak, close to $E=uB$ (for typical flow conditions $E=10$ to 20 volts/cm), thus making the plasma velocity only slightly greater than the gas velocity, the denominator in Equation 1 is dramatically decreased and efficiency dramatically improved. This electric field is too weak to sustain the plasma, and, therefore, ionization must rely on low duty cycle, high repetition rate short (on the order of a few nanoseconds), high voltage pulses. Through previous work at Princeton these pulses have been shown, to produce high efficiency plasmas. Flow acceleration would occur predominately between the ionizing pulses and substantial acceleration will require strong electric current. Estimates show that the ratio of push work to Joule dissipation (including both dissipation between the pulses and the energy deposited during the pulses) can be increased dramatically from 10^{-2} to approximately 1, while providing velocity increments of $V - V_0 = 40$ to 80 meters per second with magnetic field strengths of 3.2 Tesla and an average conductivity of 2 mho per meter, corresponding to an average electron number density, n_e, approximately equal to 2×10^{12} cm^{-3}. This newly found regime of "slow" magnetically-driven surface discharges looks very promising for boundary layer acceleration.

B. Dynamics of Plasmas Sustained by High-Voltage Repetitive Pulses

The application of MHD processes for the control of high speed air flows for application to high speed flight must rely on external methods for sustaining the conductivity because the temperature of the flow at Mach numbers less than Mach 12 is too low for thermally sustained conductivity, even if seeding is a possibility. In the externally sustained case, the air plasma is non equilibrium, and the power that is required to sustain the conductivity adds to the entropy of the flow, leading to pressure losses and degradation of the performance of the MHD system. Consequently, methods of sustaining the conductivity that are low power are of great interest.

The most efficient method of accomplishing that is to use electron beams, however, the complexity of accelerating electron beams in vacuum and passing them through aerodynamic windows suggests the consideration of other approaches. In order to achieve high efficiency, the ionizing electrons must have high energy so that they can ionize the air without losing their energy to the internal and translational modes of air molecules. The energy cost per electron is a strong function of the ratio of electric field to the molecular number density of the air (E/N). High (E/N) leads to the lowest power required to sustain the discharge. At high E/N values, however, the discharge is unstable due to runaway of the ionization. By applying a very short, high voltage pulse, however, a high electron density and a uniform discharge can be produced. The pulse repetition rate is chosen to keep the average electron density at a level sufficiently high to allow satisfactory MHD control.

To confirm the efficiency of the pulse sustained palsma, we have conducted experimental and computational studies focusing on ionization energy cost and dynamics of these plasmas in air. The experiments were performed in a polycarbonate discharge cell with aluminum electrodes (5 cm x 3 cm, separated by 3 cm) coated by a 50-micron layer of Kapton. The non-equilibrium plasma was generated at air pressures between 1 and 20 Torr by a high voltage, high frequency electrical pulser capable of generating 2.0 ns (FWHM), ~10 kV pulses across a 400 Ω load at a repetition rate of up to 100 kHz. The pulser was connected to the electrodes via a cable transformer composed of three 75 Ω coaxial cables connected in parallel at the pulser and in series at the electrodes. Current and voltage signal measurements yielded the energy deposited into the plasma in a pulse. The increase in electron number density during the pulse measured previously using microwave diagnostics was found to be 6×10^{11} cm^{-3} (±40%). Combining all uncertainties in both electrical measurements (see below) and electron number density measurements resulted in the following ranges for the energy cost of electron generation: Y_i=55-125 eV/electron at 1 Torr, Y_i=65-145 eV/electron at 5 Torr, and Y_i=70-150 eV/electron at 10 Torr.

The time-accurate modeling included diffusion-drift transport of charged species (electrons and ions) coupled with electric field-dependent electron temperature and ionization coefficients, ionization-recombination and attachment-detachment plasma kinetics, and self-consistent electric field. The model was supplemented with terms accounting for ionization due to fast ions and atoms and was calibrated against the well-known Paschen breakdown curve. (The left branch of the Paschen curve corresponds to very high values of E/N, and thus provides a good check for models of ionization in strong electric fields). In the computations, the dynamics of pulse discharge at an air pressure of p=10 Torr and the temperature of either 300 K or 600 K was modeled. The latter temperature approximately corresponds to the estimated steady-state value of average temperature in the cell after running the discharge for several minutes. The initial electron number density was 3×10^{11} cm^{-3}, corresponding to that measured in the earlier experiments. The voltage pulse shape and amplitude was taken from the measurements (Fig. 4).

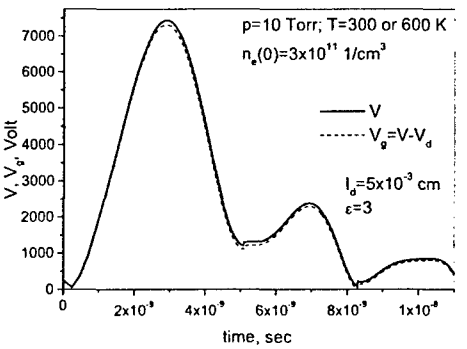

Figure 4. The experimentally measured voltage pulse on the electrodes, V, used in the computations, and the calculated voltage on the discharge gap, $V_g=V-V_d$, where V_d is the voltage drop on the dielectric layers.

Fig. 5 shows the evolution of electron number density in the middle of the gap. The electron density reaches its maximum value approximately at the moment when the absolute magnitude of voltage peaks; subsequently, the electron density experiences little change, so that the discharge only dissipates energy without producing new electrons.

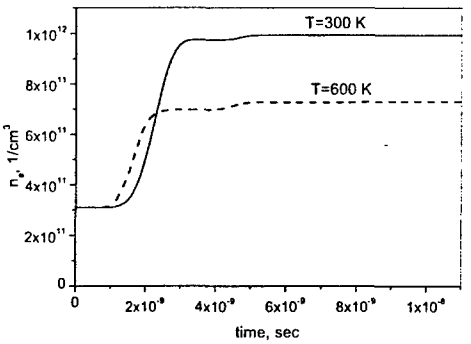

Figure 5. Computed evolution of electron number density in the middle of the gap in the case of Fig. 4.

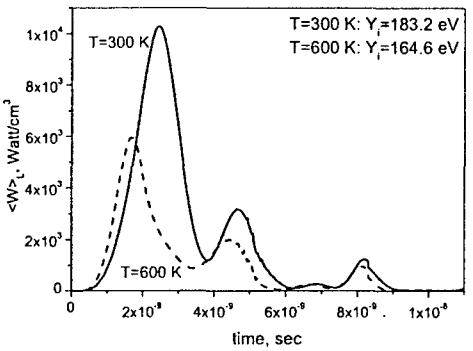

Figure 6. Computed energy dissipation rate per unit volume of the discharge as a function of time in the case of Fig. 4. The calculated energy costs per electron are shown in the upper right corner.

Therefore, from the standpoint of efficient electron generation, it would be desirable to have a pulse with a very abrupt termination, as was confirmed in subsequent parametric studies. As seen in Fig. 5, electron densities in the cases T=300 K and T=600 K differ considerably, due to the difference in gas molecule number densities in the two cases. The electron number densities, $(0.7\text{-}1)\times10^{12}$ cm^{-3}, agree reasonably well with the experimental values.

Energy dissipation rate per unit volume of the discharge as a function of time is depicted in Fig. 6. As seen in the figure, the deposited power is lower in the case of T=600 K than in the T=300 K case, corresponding to the lower number of electrons. The energy costs per electron, computed by integration of the deposited power over time and then dividing the deposited energy thus obtained by the number of generated electrons, are quite close in the two cases. Thus, the energy cost per electron weakly depends on gas density, in agreement with the experiments. The absolute value of 165 eV per electron is also in reasonably good agreement with the experimental values of 70-130 eV, given the uncertainties of both experiments and modeling.

The modeling demonstrated that the cathode sheath plays a very important role in the discharge dynamics. The sheath thickness grows as the voltage magnitude increases, reaching 0.6-1 mm at

the peak voltage. Although the sheath thickness is much smaller than the interelectrode spacing, the voltage drop across the sheath (5-7 kV) takes up most of the total voltage by the time the total voltage peaks. This creates an extremely high E/N in the sheath – higher than 10^{-13} V·cm^2, that is, more than an order of magnitude higher than the value at the Stoletov's point. An E/N that is too high makes electron generation in the sheath energetically inefficient. On the other hand, the E/N in the middle of the discharge is much lower than that in the sheath and closer to the Stoletov's point. Thus, in this high-voltage short-pulse discharge electrons are generated in the bulk plasma much more efficiently than in the sheath. This behavior is opposite to that in conventional glow discharges, where E/N in the sheath is close to the Stoletov's point and electrons are produced efficiently, while the energy cost of an electron produced in the positive column is high due to the low E/N.

C. Modeling of the Dynamics of Decaying Plasma in the MHD Section

A modeling effort was also undertaken in order to understand plasma kinetics and dynamics in the time interval between the high voltage ionization pulses. In the modeling, the flow was in the x-direction, the B-field in the z-direction, and the Faraday current in the y-direction. The modeling was quasi-1D in the y-direction. All calculations were performed for the experimental conditions: p=10 Torr; T=106 K; u=620 m/s; B=5 T. The spacing between the MHD electrodes was 3 cm.

The results of modeling for a Faraday generator with continuous electrodes are shown in Figs. 7-10. Due to the weak electric field, the electron temperature in the decaying plasma is very low, as seen in Fig. 7. The collision rate of the low-energy electrons is correspondingly low, leading to both high scalar conductivity and high Hall parameter. Therefore, the effective electron conductivity, $\sigma_{eff} = \sigma/(1+\Omega^2)$ is quite low. Perhaps the most surprising result for these unusual conditions is shown in Fig. 8: the cathode voltage fall does not exceed a few volts. This is because the high value of Hall parameter inhibits the motion of the electrons.. In fact, as seen in Fig. 9, the electron conductivity becomes so low that the electron current is comparable to the ion current. This eliminates the principal reason for a substantial cathode fall (the large difference between electron and ion mobilities).

Since the cathode fall is insignificant, the decrease of the current with time after the pulse is due to the bulk losses of electrons and ions in recombination and attachment. Both recombination with cluster ions and three-body attachment to oxygen make comparable contribution to the experimentally observed decay rate.

As seen in Fig. 10, the computed decay of the current for the initial value of n_e of 5×10^{11}-10^{12} cm^{-3} agrees well with the experimental data. This means that the peak value of $n_e = 5\times10^{11}$-10^{12} cm^{-3} was reached in the experiments. The absolute value of the peak current density, 0.2-0.4 mA/cm^2, together with the estimated effective current-collection area of a few cm^2, is in good agreement with the experimentally measured peak current.

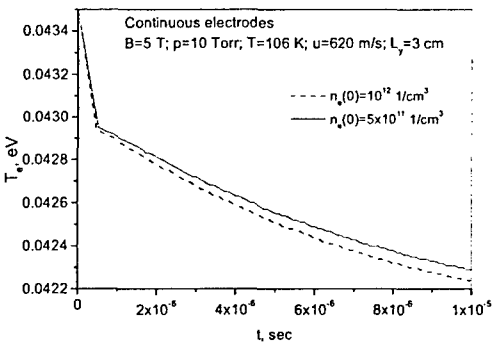

Figure 7: Electron temperature after the pulse in the Faraday generator with continuous electrodes.

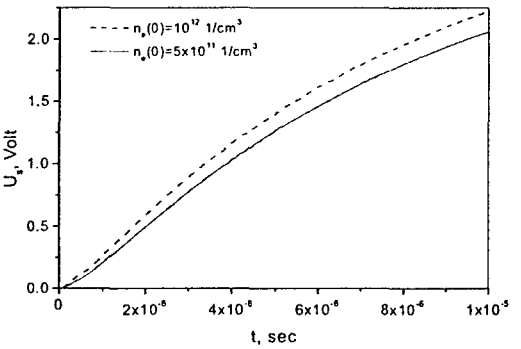

Figure 8: Cathode sheath voltage fall after the pulse in the Faraday generator with continuous electrodes.

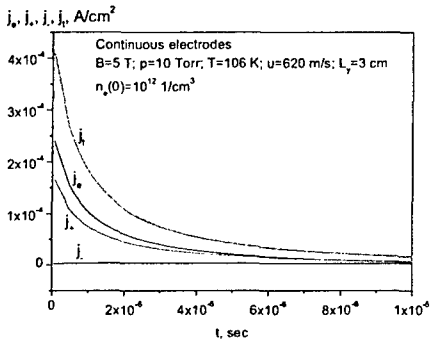

Figure 9. Current densities in the mid-plane between the electrodes (y=L_y/2): electron current, j_e, positive ion current, j_+, negative ion current j_- and the total current, $j_t = j_e + j_+ + j_-$, calculated in the assumption k=0, at two different values of initial (peak) electron density in the Faraday generator with continuous electrodes.

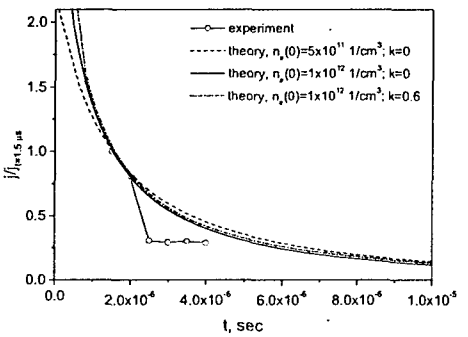

Figure 10: Comparison of the calculated normalized current density for continuous-electrode Faraday generator with experiment.

Modeling was also performed for an ideal segmented-electrode Faraday generator. The results, shown in Figs. 11 and 12, are dramatically different from the continuous-electrode case. The Faraday current is initially strong, and the relatively strong Faraday electric field in the channel heats the electrons (Fig. 11). This results in the rapid (on 10-nanosecond time scale) growth of cathode voltage fall, depicted in Fig. 12. The rapid growth of the cathode sheath leaves very little voltage for the quasi-neutral plasma, and the current drops very quickly, even with little recombination and attachment. This should be taken into account when planning experimental work with segmented-electrode MHD devices.

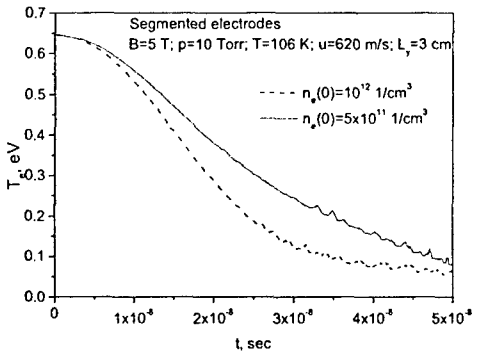

Figure 11: Electron temperature after the pulse in the ideal Faraday generator with segmented electrodes and k=0.

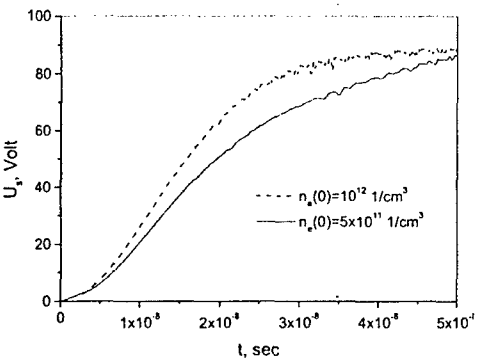

Figure 12: Cathode voltage fall after the pulse in the ideal Faraday generator with segmented electrodes and k=0.

D. Power Extraction by MHD in Cold Air

A small-scale Mach 3 wind tunnel has been built to demonstrate MHD power extraction from cold supersonic air. The tunnel test section is placed in a uniform 6 Tesla magnetic field, and the conductivity is sustained by a 100 kHz, 30 kV, 2 nanosecond pulse generator that is capacitively coupled into the air flow. The discharge is struck along the magnetic field lines which tend to stabilize it. The MHD device is run in the Faraday configuration, so the MHD current flows orthogonal to the magnetic field and to the flow velocity. The static pressure of the test section is 12 Torr and the static temperature of the flow is 106K. The flow velocity is 600 m/s, and the cross sectional dimensions are 2.0" by 1.2", with the high voltage pulses applied across the 1.2" dimension. The pulser electrodes are shielded from the flow by a thin dielectric layer so that the MHD voltage, which is developed in the orthogonal direction, is not shorted out. The high voltage pulser electrodes do not extend to the side walls, but occupy the central 1.2" of the channel so that the discharge does not enter the side boundary layer regions, otherwise the discharge forms primarily in the boundary layer where the density is lower than in the core region and the temperature is higher. Figure 13 shows an end on diagram of the pulser electrodes and the corresponding glow discharge.

The electron number density was measured in a static cell with under similar dimensions and E/N conditions, but not in a magnetic field. The measurement was made by attenuation of a 12.6GHz microwave that was launched and collected by a horns placed on either side of the cell and detected through a low noise amplifier. Figure 14 shows the measured attenuation as a function of time at two cell fill pressures. In order to convert this measurement to the electron number density, the collision frequency of the electrons with air molecules must be taken into account. That is a function of both the electron energy and the number density. Since the energy of the electrons is rapidly changing after the pulse, the effects of the collisions are not easily determined. Figure 15 shows the transmission vs electron number density for different collision frequencies. Our measurements were at 9 Torr and 15 Torr corresponding to collision frequencies of 2.7

GHz, and 4.5 GHz. With that approximation we can invert the absorption data to get the time variation of the electron number density shown in figure 16.

For the measurements of power extraction in the wind tunnel, the channel has to be fitted with MHD electrodes that extract current in the direction orthogonal to both the flow and the magnetic field. Since the discharge does not reach the walls, the MHD electrodes are 0.5" long thin plates that extend into the discharge region from the walls and are streamlined so that they do not generate significant shocks. In order to observe the current and avoid parasitic effects from wires, a photo diode is placed across the MHD electrodes and the diode output is monitored by an optical detector coupled through a 10 meter optical fiber. The current flowing through the plasma as a function of time is then monitored by the photo diode as shown in Figure 17 . That diode was set up so that only current flowing in one direction was observed by the photodetector.. When the magnetic field was switched, the same current flowed, but in the reverse direction. The observation of only one direction allowed us to eliminate parasitic effects from the pulser and other noise sources. Figure 18 shows the resulting current, confirming that MHD power extraction is occurring. This is the first known demonstration of MHD power extraction from supersonic cold air.

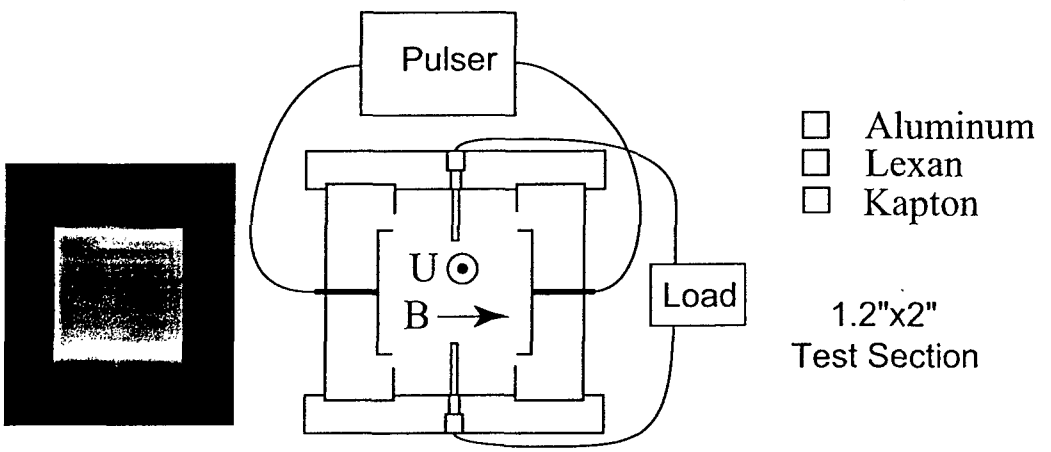

Figure 13: Pulser sustained glow discharge in Mach 3 flow with 12 Torr static pressure and 106 K static temperature (left) and cross section of the MHD channel showing the high voltage pulser electrodes confined to the central portion of the channel to avoid excitation of the boundary layers (right).

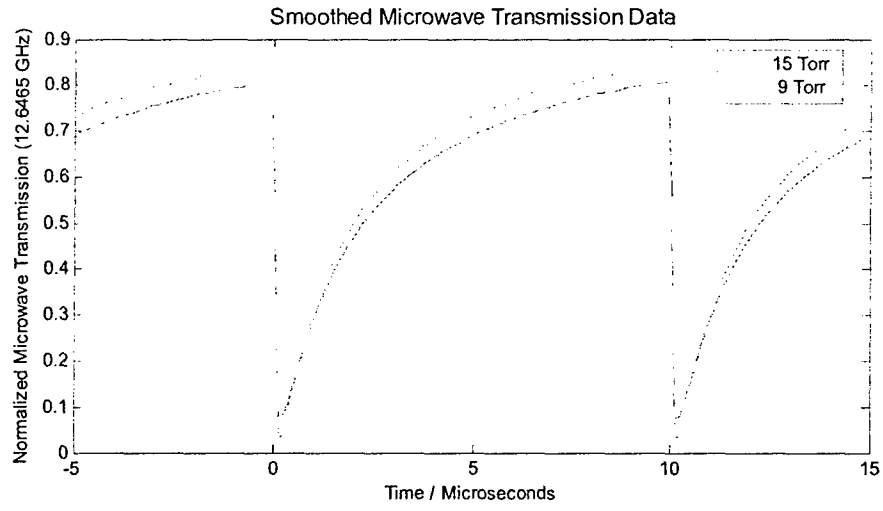

Figure 14: The microwave transmission through our static cell – 3 cm plasma thickness.

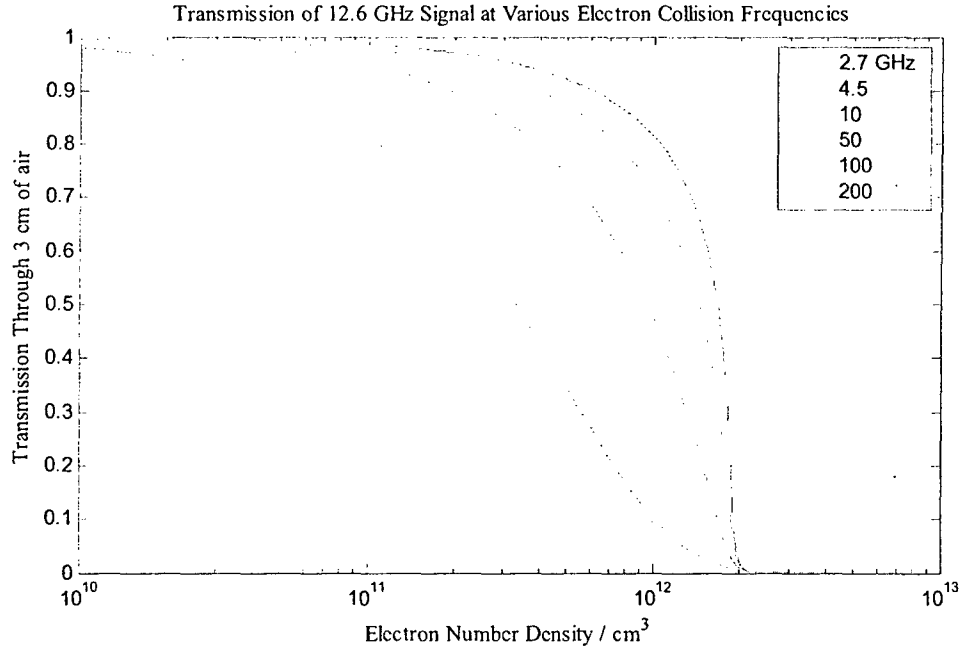

Figure 15: Calculated transmission through 3 cm of material with electron collision frequencies ranging from 2.7 GHz to 200 GHz. A collision frequency of 0.3 GHz / Torr applies to most of our measurement time, so measurements at 9 Torr and 15 Torr correspond to approximately 2.7 GHz and 4.5 GHz.

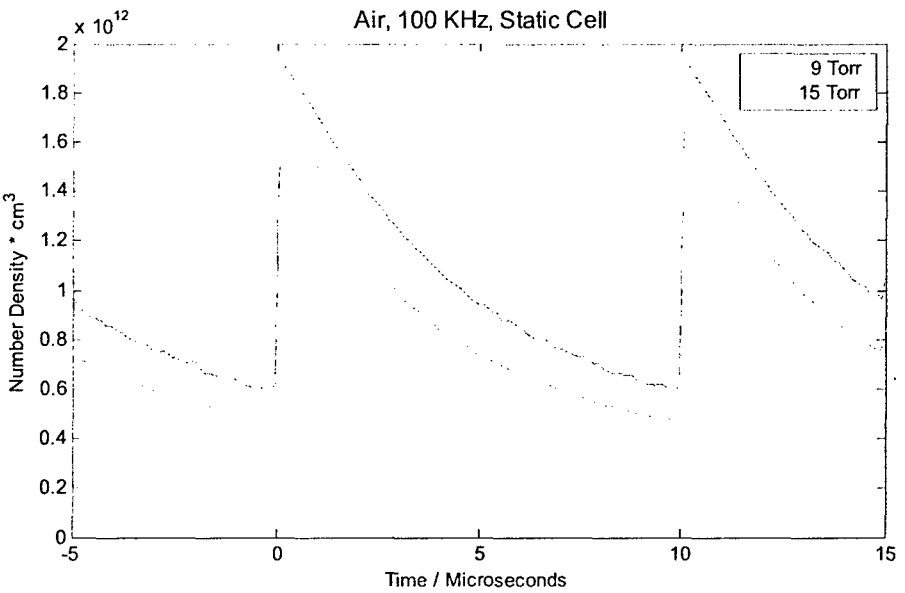

Figure 16: The resultant electron number densities as a function of time for the two static cell pressures

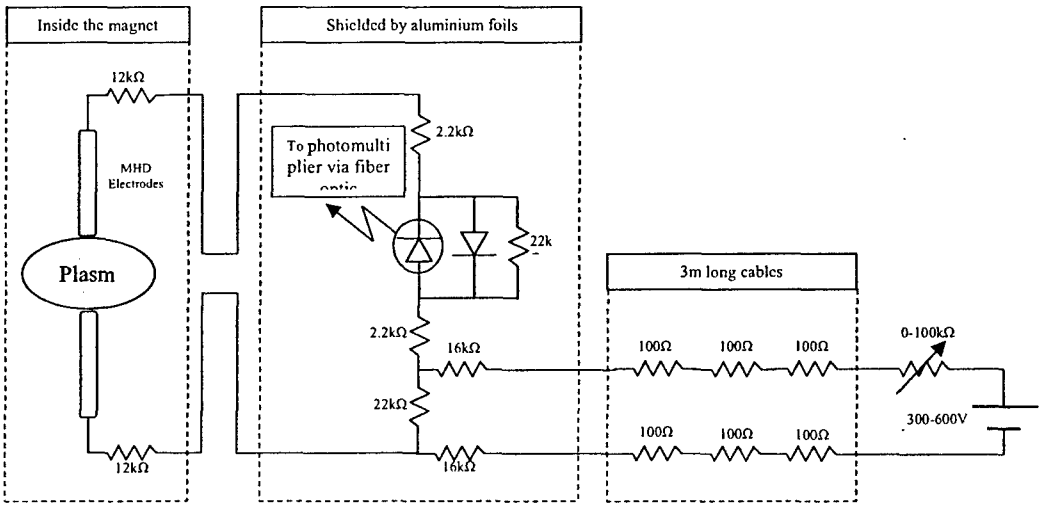

Figure 17: Electric circuit for the voltage bias application and the current measurement. The photo diode emits light proportional to the current flowing through it and that light is detected 10 meters from the experiment by optical fiber coupled photo detector.

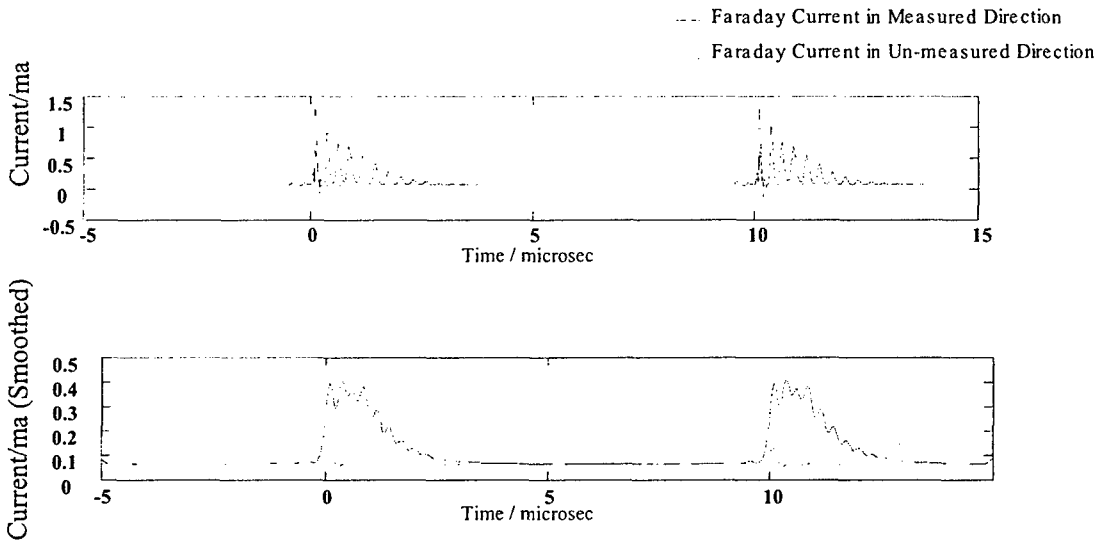

Figure 18: Measured MHD current in the forward (blue) and in the reverse (green) directions. The lower curve is smoothed to remove the pulser induced oscillations.

E. Modeling of Hypersonic Aerodynamic Control and Thrust Vectoring by Nonequilibrium MHD Devices

Using our plasma/MHD models (including Hall and ion slip effects and ionization by electron beams), a theoretical investigation of hypersonic aerodynamic control with cold-air MHD devices has been conducted. Arrays of MHD devices can be positioned at the bottom of the vehicle aft of the combustor, where the density is close to that in the freestream, and/or on the top of the vehicle. In the modeling, the cold hypersonic flow was assumed to be ionized by electron beams injected along the magnetic field lines. The strength of magnetic field was a decreasing function of the distance along its direction from the surface; the function was that of the magnetic field along the axis of a coil with the radius R_M=0.5 m, and the maximum magnetic field strength (at the surface) was B_0=3 Tesla. The magnetic field was assumed uniform in both x and y directions. The plasma region had the length $\Delta x_{MHD} = 0.15$ m along the flow, and the electron beams were assumed to have such an energy spectrum that the beam-induced ionization rate is uniform in the entire plasma region, from the vehicle surface to the distance L_b=0.65 m from the surface. Depending on the flow parameters, the maximum electron beam energy was $\varepsilon_b \le 25$ keV, and the beam current density varied from $j_b \sim 260$ A/m^2 to $j_b \sim 1300$ A/m^2. The $\vec{j} \times \vec{B}$ accelerating or decelerating forces together with the Joule heating of the flow can ensure both angle-of-attack and steering control. The tangential forces were shown to vary dramatically with the ratio χ of the applied electric field to the product of freestream velocity and the magnetic field at the surface. Computations for Mach 8

demonstrated how the profile of $\vec{j}\times\vec{B}$ forces changes with χ, from predominantly decelerating forces (drag) at low χ to a combination of deceleration near the surface and acceleration of the outer flow at $\chi\approx 0.5$, to only acceleration (thrust) at $\chi=1$ (Fig. 19).

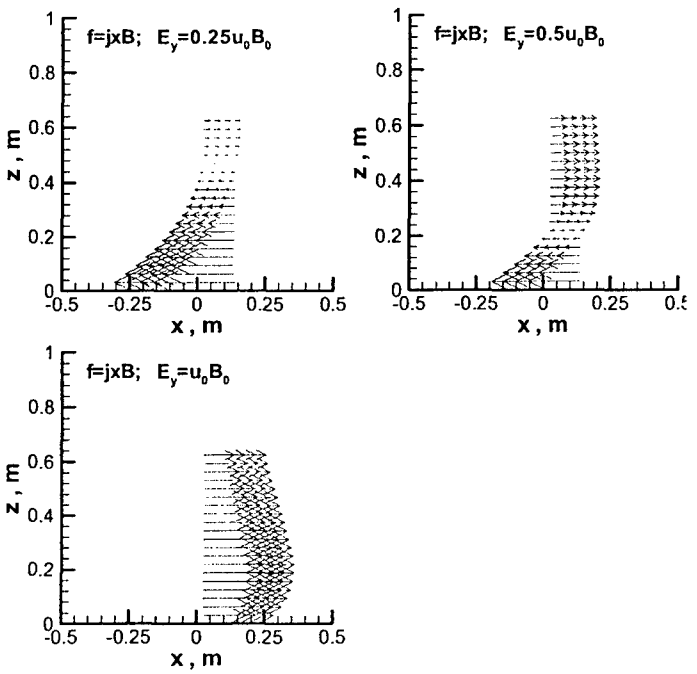

Figure 19. Profiles of $\vec{j}\times\vec{B}$ forces at $\chi = E_y/u_0B_0 = 0.25$ (upper left plot), χ=0.5 (upper right plot), and χ=1 (bottom left plot), at Mach 8, q=1000 psf. Magnetic field tilt angle is $\alpha=\pi/2$, and e-beam power deposition density is Q_b=10 MW/m^3.

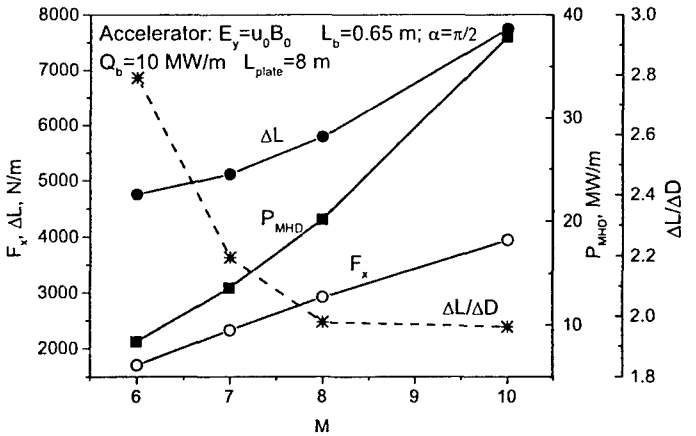

Figure 20. Thrust (F_x) and lift (ΔL) forces, their ratio ($\Delta L/\Delta D$), and the MHD deposited power versus Mach number for MHD accelerator with χ=1, tilt angle $\alpha=\pi/2$, and the electron beam power density Q_b=10 MW/m^3.

Varying the tilt angle α of the magnetic field was shown to increase the flexibility of MHD control. The normal (lift) force created by the MHD region turned out to be substantially stronger than the drag/thrust force, with the lift-to-drag (for MHD generators) or lift-to-thrust (for accelerators) ratios increasing from about 2 with magnetic field tilted against the flow or normal to the surface to more than 3 with aft-tilted magnetic field. Computations performed for representative generator and accelerator cases in the range of Mach numbers from Mach 6 to Mach 10 revealed that, while both tangential (drag – for generators, and thrust – for accelerators) and normal (lift) forces tend to increase with Mach number, the lift-to-drag (for MHD generators) or lift-to-thrust (for accelerators) ratios monotonically decrease with Mach number (Fig. 20).

II. NON-MHD FLOW CONTROL AND POWER EXTRACTION

A. Virtual-Shape Inlet Control: Assessment of the Performance of Reverse Energy Bypass Concept

If sufficient power is available on a hypersonic vehicle, that power can be applied to either a virtual cowl, which deflects air into the inlet, enhancing the performance of the vehicle (Fig. 21), or to a system that introduced heat into the inlet flow to reduce the Mach number and eliminate the isolator (Fig. 22). A theoretical study was performed to determine whether these configurations can improve the overall performance of an accelerating vehicle passing through Mach numbers below the design cruise Mach number. Parameters of an MHD generator placed downstream of the combustor were calculated for conditions corresponding to Mach 5 for the isolator elimination and Mach 6 for the virtual cowl flight at q=1000 psf with the one-dimensional model.

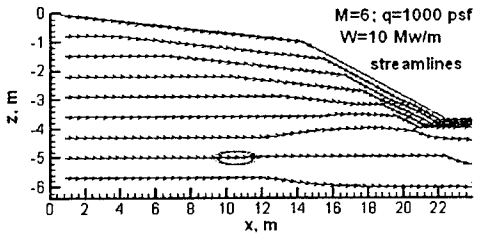

Figure 21: Virtual Cowl.

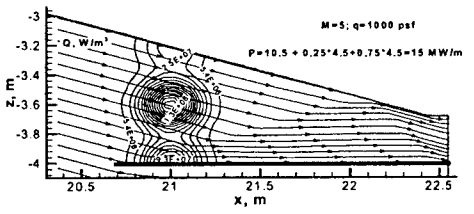

Figure 22: Power deposition in the inlet for elimination of isolator.

From the model it was found that seed fractions of 1% and 1.5-3.4 Tesla magnetic fields in the exit of the SCRAM engine can produce more than enough power to heat the flow upstream of the inlet and eliminate the need for an isolator duct (at least 20 MW/m), and to operate a virtual cowl for mass capture increase (at least 10 MW/m). This configuration is called the reverse bypass, where power is extracted downstream of the engine and used for modifications of the inlet flow. Assuming a 52% power transfer efficiency from the MHD section to the air entering the inlet duct, the heating in the duct leads to a decrease of the thrust by 16%. This is a relatively small penalty for the removal of the isolator, since this will lead to lower weight and reduced heat loads at cruise speeds. Assuming a 25% efficiency in power delivery to the ideal location upstream of and below the inlet (see Fig. 21), an overall increase in thrust of between 5% and 9% is predicted for the virtual cowl.

The best performance for the reverse energy bypass with an optimally located virtual cowl is 9.4% thrust increase, while thrust increase with the virtual cowl close to the cowl lip is 6.5% (assuming only 50% microwave efficiency). The choice between the two scenarios would involve a trade-off between performance and practicality.

B. Dielectric Barrier Discharge

There has been much interest in the dielectric barrier discharge for the control of separation on airfoils, but there is little understanding of the physical processes that cause the surface jet to occur when such a discharge is formed. We have undertaken an experimental and theoretical effort to clarify that physics. The dielectric barrier configuration is shown in Fig. 23. An exposed upper electrode is paired with an insulated electrode located under a thin dielectric and an RF discharge is struck between the two. It has been observed that this discharge generates a surface jet in the direction indicated in the figure. We have undertaken a detailed modeling effort to understand the origin of this surface jet and propose an optimized wave form for increasing the surface jet velocity.

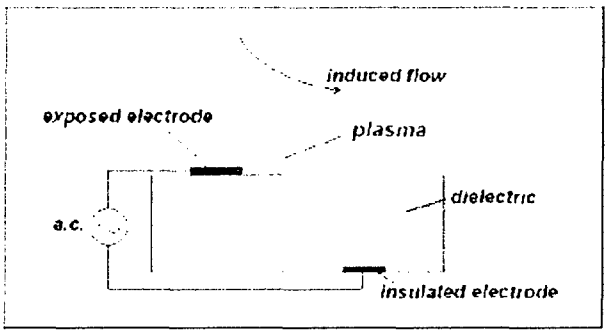

Figure 23. Dielectric barrier discharge configuration.

Our modeling indicates that charging of the dielectric occurs during the time the exposed upper electrode is negative, causing a field gradient to be established which subsequently drives the positive ions in the downstream direction. These ions then couple to neutral air and create the jet. The problem with the sinusoidal-varying potential is that there are significant reverse forces that arise.

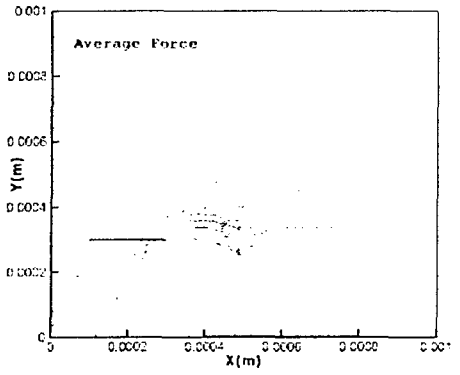

Figure 24. Average forces from a sinusoidal applied voltage

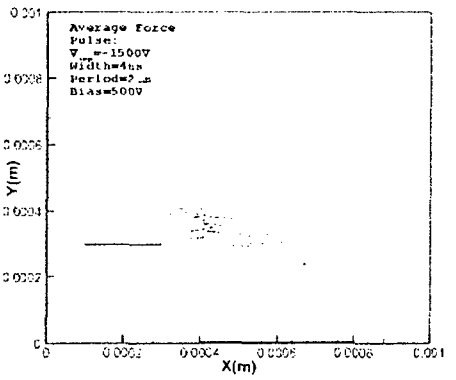

Figure 25. Average forces from a high voltage pulsed applied voltage

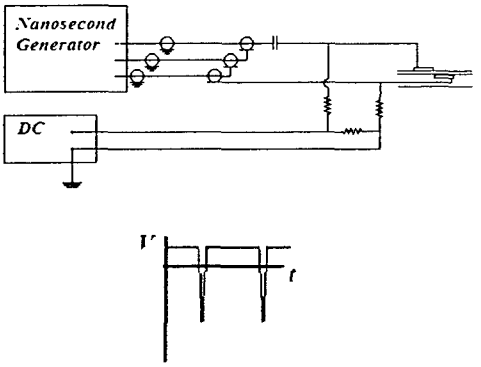

Figure 26: Schematic of pulse generator and DC driven dielectric barrier discharge

Figure 24 shows the average force near the exposed electrode for an applied sinusoidal voltage. From the large-scale, left pointing vectors at the lower-left part of the diagram it is apparent that this reverse force significantly decreases the effectiveness of the device. Our modeling has indicated that, with the application of a very short, negative high voltage pulse to generate the ionization, and a positive DC bias, this reverse effect can be suppressed and a larger average downstream velocity generated, as shown in Fig. 25. The challenge in the modeling and understanding the dielectric varying discharge plasma actuators stem from the physics of the problem. The ability of this new model to capture the important physical phenomena has provided a useful capability for this optimization effort. Work on this program has been jointly supported by Boeing (St. Louis).

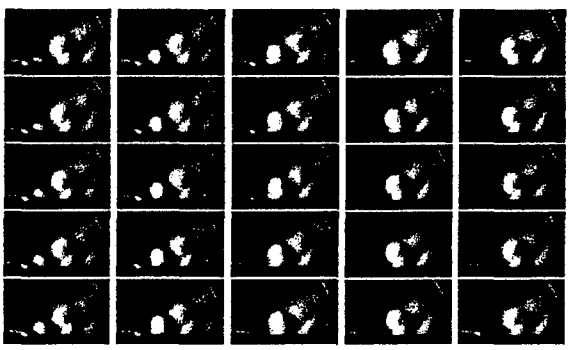

Figure 27: Asynchronous shadowgraph images of the pulsed DBD surface jet. Frames are top to bottom, left to right.

A dielectric barrier discharge driven by a nanosecond pulse generator and dc bias, as shown in Fig. 26, has been built. The nanosecond pulse generator is operated in a burst mode in order to provide contrast for Schlieren measurements of the jet created by the dielectric barrier discharge. Figure 27 shows an asynchronous movie of the jet generated by the dielectric barrier discharge. The frames proceed from top-to-bottom, left-to-right. The velocity of the structures is on the order of 25 m/sec, increasing by almost a factor of two with the DC bias. This diverging structure is driven by the small-scale surface jet in proximity to the barrier discharge. That jet will have much higher velocity then this large-scale downstream structure. Work is on-going to measure that velocity and (with Dr. Jon Poggie at AFRL) to development parallel architectures for the code and expand the code capabilities.

C. Thermionic Power Conversion

Large temperature gradients occur between surfaces exposed to high temperatures associated with engines and/or high speed flight and the structure elements that support those materials. It would be attractive to find a way of converting a significant portion of that heat into electricity, not only for applications on board a vehicle, but also for augmenting cooling. From our modeling work, we believe that an efficient two-dimensional thermionic panel can be built and operated with an internal plasma sustained by high voltage pulses.

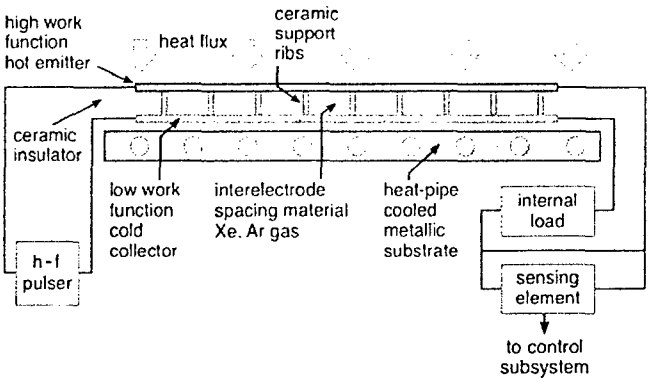

Figure 28: Diagram of thermionic surface panel for power extraction and enhanced cooling

Two types of thermionic devices have been previously examined: a narrow gap configuration and a cesium vapor-filled ignited mode configuration. In the first case, to avoid significant current reduction by space charge build-up, very small interelectrode gaps on the order of a few microns are required. These are impractical for structural elements, however, recent work on nanoscale thermionic devices may provide some new capabilities in this area. More commonly, space charge is overcome by a discharge that is sustained in few millimeter interelectrode gap filled with cesium vapor. Cesium is chosen because of its low ionization potential, but it adds complexity to the configuration since the vapor pressure of the cesium must be controlled by a low temperature reservoir that may not be easily incorporated into an extended panel configuration. The use of an inert gas together with high voltage pulses relieves the need for a low temperature reservoir and opens up the opportunity for a two-dimensional device. A diagram of such a device is shown in Fig. 28. Figure 29 shows the power expended in the generation of electrons for 1000 K argon at various pressures in a 5 mm gap device. This power is sufficient to sustain 10 amps/cm^2 of current, and, averaged over the pulse repetition rate, corresponds to only a few percent of the power generated by the device itself. Because of the small separation between electrodes, the high voltage pulses only correspond to voltages of a few tens of volts. Experimental work is planned over the next year with additional support from the Air Force Research Laboratory.

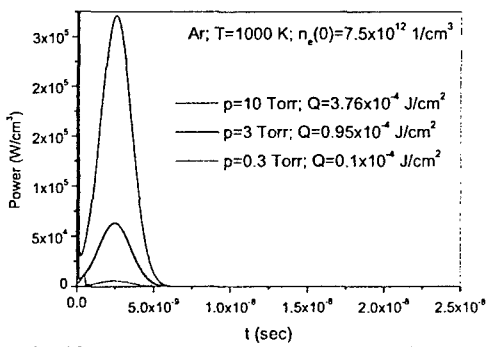

Fig. 29 Power expended in the generation of electrons in the gap by high field, nanosecond pulse.

III. New Diagnostics

A. Magnetically Modulated Microwave Attenuation for Diagnostics of Short Pulsed Sustained Plasmas in a Cold Air MHD Channel

Figure 30 describes the estimated 12.64 GHz microwave transmission for the extraordinary polarization (across the magnetic field lines) case as a function of electron number density for various values of collision frequencies and magnetic fields. Note that, at 0.4 Tesla, the microwave will be completely absorbed for a small window of electron number densities. The absorption curve broadens as the collision frequency is increased. The complete absorption occurs for the case where the sum of the squared plasma frequency and the squared cyclotron frequency becomes equal to the square of the microwave frequency ($\omega_p^2 + \omega_h^2 = \omega^2$). The plasma frequency at 0.4 Tesla is around 11 GHz, whereas the cyclotron frequency at this magnetic field is about 5 GHz. For the experiment a 12.64 GHz microwave was passed through a pulsed plasma maintained in a static cell, which was place in a magnet capable of reaching 6.5 Tesla. The experimentally measured extraordinary transmission is shown in Fig. 31. It clearly indicates almost no transmission for 0.4 Tesla magnetic field at various cell pressures. Figure 32 shows that for collision frequencies above 10 GHz, the transmission at 0.4T begins to increase again. This implies that the collision frequency of the plasma in the static cell lies between 2 to 10 GHz, and the electron number density falls between 2×10^{11} to 7×10^{11} cm^{-3}. It is important to note that the collision frequencies inferred from the data are low but are consistent with the electron mobility and electron collision frequency expected at electron temperature of the order of 0.1 eV or lower (see the next section). The relaxation time for high temperature electrons following the 2 nsec high voltage pulse is of the order of submicroseconds, and after that period, electron temperatures drop at a dramatic rate. The measured current, voltage, power and deposited energy are shown in Fig. 33. From that measurement and from our knowledge of the electron number density, we estimate that the cost per ionized electron is 100 eV. That is in close agreement with predictions and only three times the absolute minimum achievable with an external electron beam.

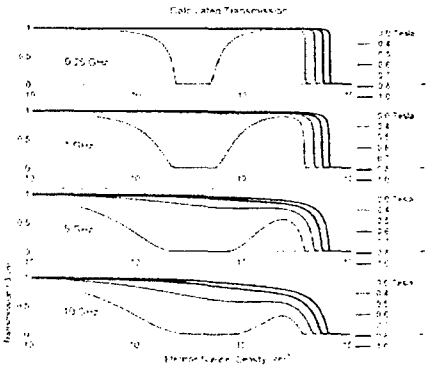

Figure 30: Calculated extraordinary trans-mission as a function of electron number density for various collision frequencies.

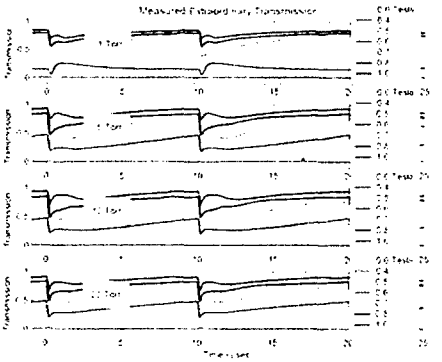

Figure 31: Measured extraordinary trans-mission at various magnetic field levels with different cell pressures (pulser operating at 100 kHz rate).

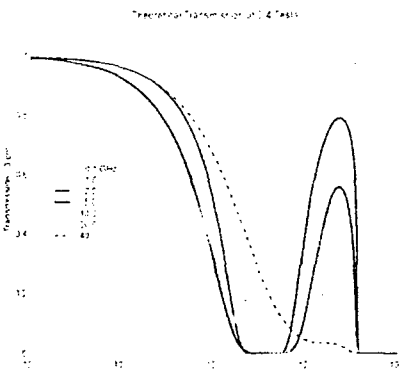

Figure 32: Calculated extraordinary transmission as a function of electron number density at 0.4 Tesla with various collision frequencies.

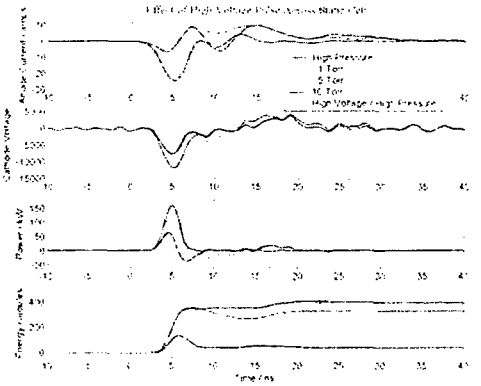

Figure 33: Measured current, voltage power and deposited energy in static cell from nanosecond high voltage pulser.

B. Radar REMPI

We have undertaken the development of a new diagnostic approach for the measurement of electron number density based on the scattering of microwave radiation from a small laser-induced plasma. The laser is tuned to a wavelength that produces a very small plasma through resonant-enhanced, multiphoton ionization, and this plasma is observed by microwave scattering. Due to the high sensitivity of the microwave detection and its direct relationship to the density of charges, the whole lifecycle of the laser-induced plasma can be measured from the initial stages of ionization during the nanosecond laser pulse, through the growth of the spark evolution, and finally the loss of charge through recombination and attachment. The resonant-enhanced nature of the laser-generated ionization provides the capability of using this technique for spectroscopy by frequency tuning the laser. By observing the rate of recombination, particularly for very weak sparks, this approach may provide a new method for the measurement of temperature. Of particular interest for this work is the potential for using the rise time of the pulse to determine the ambient electron number density. The geometry of the scattering is shown in Figure 34. Modeling of a true laser pulse indicates that the electron number density increases in an exponential fashion during the rise time of the laser pulse, reaching significant ionization in a time related to the initial electron number density and the fluence of the laser. Figure 35 shows the different rise times associated with different laser pulse energies all focused to the same focal volume. By observing the time between the initial turn-on of the laser pulse and the observation of the microwave

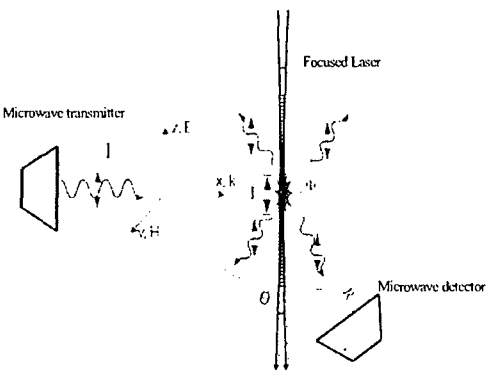

Figure 34: Radar REMPI configuration

scattering, it may be possible to extract the initial electron number density. Work is currently on-going to examine this possibility.

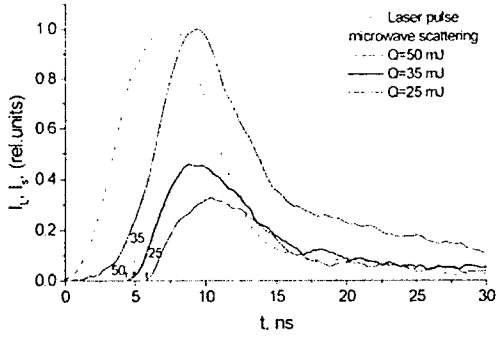

Figure 35: Measured Radar REMPI signal in air at pulse energies showing the delay in rise time associated with pulse energy. Arrows are from Figure are predictions based on the laser pulse shape.

IV. Acknowledgment/Disclaimer

This work was sponsored (in part) by the Air Force Office of Scientific Research, USAF, under grant/contract numbers F49620-03-1-0028. The views and conclusions contained herein are those of the authors and should not be interpreted as necessarily representing the official policies or endorsements, either expressed or implied, of the Air Force Office of Scientific Research or the U.S. Government.

V. Personnel Supported During Duration of Grant

Richard B. Miles	Professor, Princeton University
Sergey O. Macheret	Senior Research Scientist, Princeton University
Mikhail Shneider	Research Scientist
Sohail Zaidi	Research Scientist
Philip Howard	Technical Support
Robert Murray	Graduate Student (partial support) Currently at General Electrics Research Laboratory
Lipeng Qian	Graduate Student (partial support)
Xingguo Pan	Graduate Student (partial support) Current Position: Graduated, Ph.D. Currently employed by Morgan Stanley, New York, NY
Brendan McAndrew	Graduate Student (partial support) Current Position: Graduated, Ph.D. Currently employed as a Post-Doc, George Washington Univ., Washington, DC

VI. Visitors Affiliated with the Project

Leonid Vasilyak	Visiting Research Scientist, Russian Academy of Sciences
Walter Beck	Visiting Research Scientist, DLR, Gottingen, Germany

VII. STUDENT THESES

A. Xinggau Pan (Ph.D. November 2003)
Coherent Rayleigh Brillouin Scattering

Executive Summary

This thesis developed a new diagnostic approach that used a nonlinear interaction of counterpropagating laser beams to modulate the density of either an atomic or a molecular gas. Figure A.1 shows a diagram of the interaction zone. The two pump beams, pump 1 and pump 2 produce a standing wave intensity distribution. When the frequency of these two beams are slightly different, the standing wave pattern moves. Due to the ponderomotive force, the atoms and molecules are attracted to the high intensity regions. By scattering a probe beam off of the modulated density distribution, a counterpropagating signal is generated. The strength of this signal is proportional to the number of atoms or molecules contributing to the modulation and their polarizability. When the standing wave pattern moves, it couples to those molecules that are moving at close to the same velocity. The signal as a function of the standing wave motion can be quantitatively related to the temperature and pressure through a kinetic theory that is developed in the thesis. Figure A.2 shows the predicted distribution (solid lines) and the measured signal for argon. Since the interaction region is localized to within the focal volume of the overlapping laser beams, this can be used as a measurement of local temperature and pressure. This technique can be applied to either atomic or molecular gases. The coherent interaction produces a directed signal beam that remains strong even from low density gases.

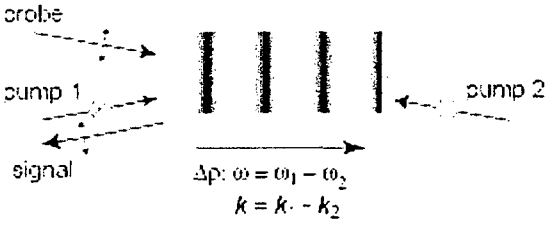

Figure A.1. Diagram of the interaction zone showing the counterpropagating pump lasers that generate a standing wave density distribution that scatters a probe beam creating a coherent backward propagating signal beam. The density distribution moves at a speed related to the frequency difference between the two probe beams, and that produces a Doppler shift in the signal.

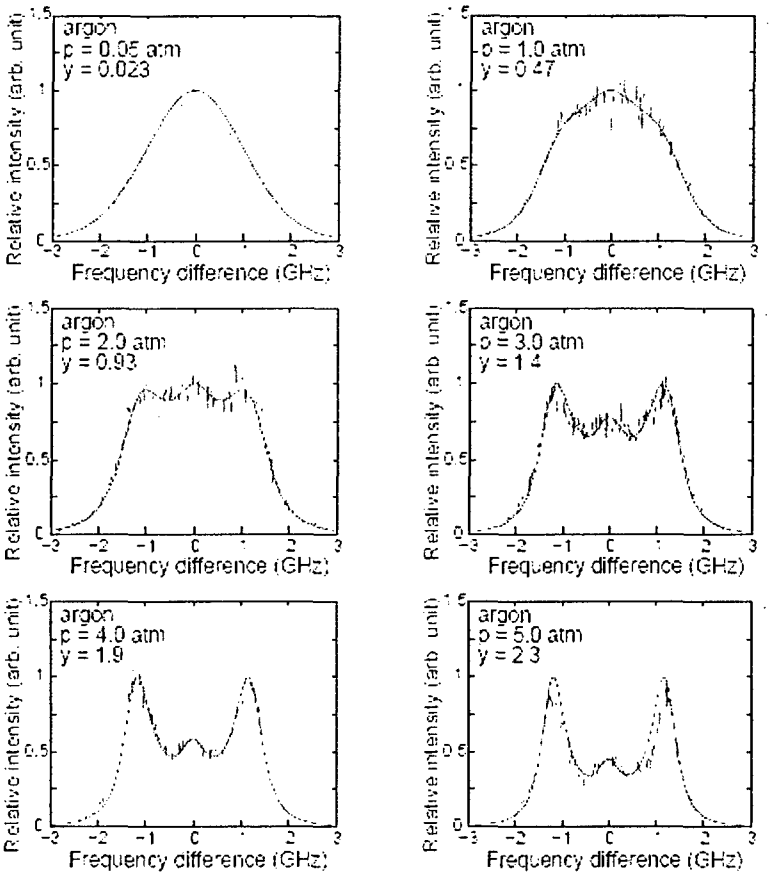

Figure A.2. Comparison of kinetic theory predicted and measured Coherent Rayleigh Brillouin Scattering for argon at 292K, at various pressures showing the change in the character of the scattering due to the influence of acoustic waves and higher pressure.

B. Brendan McAndrew (Ph.D June 2004)
Aerodynamic Control in Compressible Flow Using Microwave Discharges

Executive Summary

This thesis explores the use of a discharge in front of a supersonic vehicle for the reduction of drag and the generation of lift. The experiment was performed in Mach 3 indraft air tunnel that was configured as a tapered microwave waveguide. The tapered guide ended with an opening that was smaller that the cutoff dimension, so that the microwave field was reflected and a standing wave was formed. A contoured nozzle was made of Teflon and inserted into the tapered guide such that the test section was at the microwave cutoff location. In this manner a discharge could be localized just upstream of the model, in front of the bowshock. The tunnel configuration is shown in Figure B.1.

The model is a conical sharp tip nose that is mounted such that strain gauges can measure the drag and lift. Figure B.2 shows a cross section of the model. Figure B.3 shows the structure of the discharge in the tunnel. The discharge is stabilized against the wall and curves downstream into the center of the tunnel where the field is highest. Because of the wall stabilization, the discharge is off center, so the energy added to the supersonic flow not only reduces the drag, but it creates lift. Figure B.4 is a photograph of the discharge in the tunnel, and Figure B.5 shows the measured lift and drag reduction as a function of microwave power.

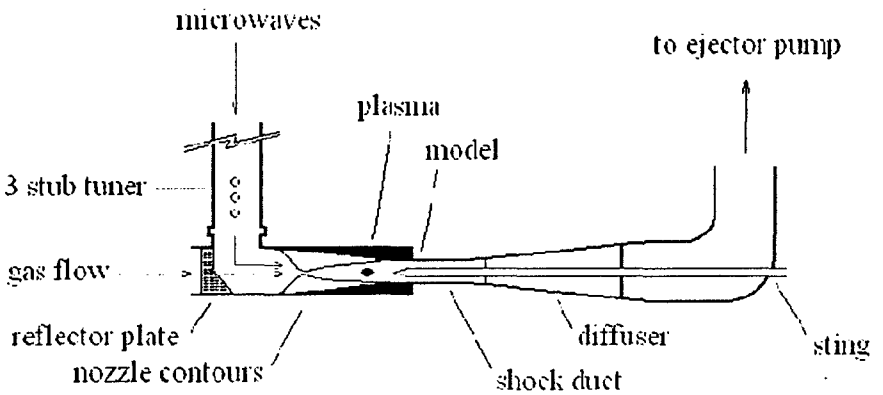

Figure B.1. Wind tunnel configuration with a porous microwave reflection plate located in the plenum and a tapered waveguide surrounding the Teflon nozzle. The taper exit at the model location is below the cutoff dimension of the waveguide, so a standing wave microwave field is produced in the region upstream of the model bow shock.

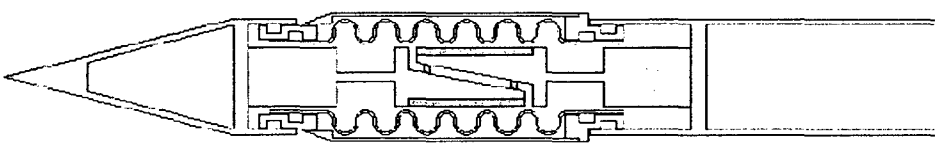

Figure B.2. Model cross section showing the location of the strain gauges for the measurement of lift and drag.

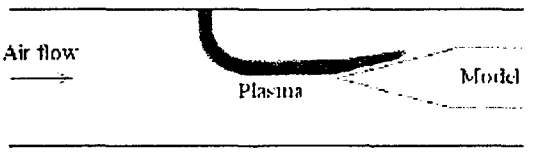

Figure B.3. Wall stabilized discharge sustained by microwave field such that the discharge is located upstream of the model. The discharge is off center so that lift is generated.

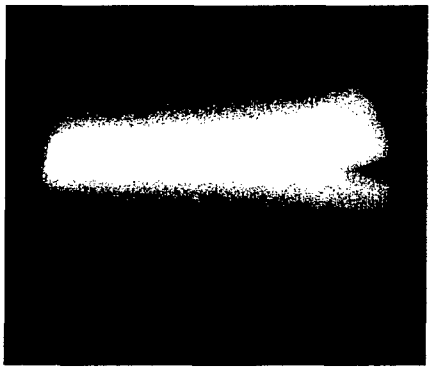

Figure B.4. Image of the microwave sustained discharge inside the wind tunnel showing the nose tip of the model. Flow is from left to right.

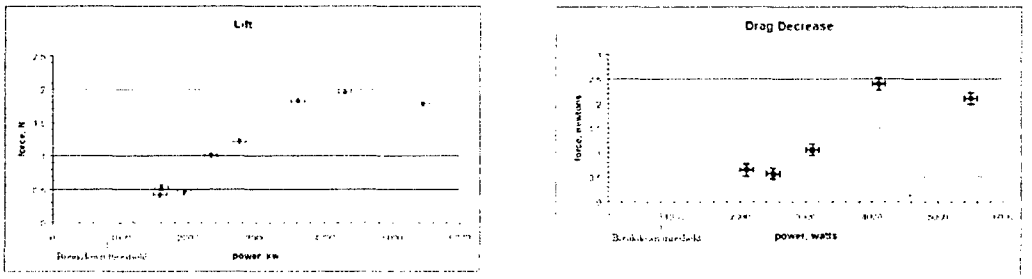

Figure B.5. Measured Lift and Drag decrease as a function of microwave power.

C. Robert C. Murray (Ph.D June 2005)
First Demonstration of MHD Power Generation Using Externally Ionized, Cold, Supersonic Air as a Working Fluid

Executive Summary: This work is summarized in sections I.D and III.A of this final report.

VII. PUBLICATIONS AND TECHNICAL PAPERS

I.G. Girgis, M.N. Shneider, S.O. Macheret, G.L. Brown, and R.B. Miles, "Steering moments creation in supersonic flow, by off-axis plasma heat addition," J. Spacecraft and Rockets 43 (3): 607-613 MAY-JUN 2006

M. N. Shneider and S.O. Macheret, "Hypersonic Aerodynamic Control an Thrust Vectoring by Nonequilibrium Cold-Air Magnetohydrodynamic Devices", J. Propulsion and Power, 22, #3, (May-June 2006), pp 490 – 497.

R.C. Murray, S.H. Zaidi, S.O. Macheret, and R.B. Miles, "Microwave diagnostics of a repetitive, short-pulse-sustained, weakly ionized, air plasma under the influence of a magnetic field," IEEE Trans. On Plasma Sci. 34 (3): 1004-1012 Part 3 JUN 2006

M. Zheltikov, M. N. Shneider, and R. B. Miles, "Radar Return Enhanced by a Grating of Species Selective Multiphoton Ionization as a Probe for Trace Impurities in the Atmosphere", Applied Physics B – Lasers and Optics 83 (1): Apr 2006, pp 149-153.

R. C. Murray, S.H. Zaidi, and R. B. Miles, "Magnetohydrodynamic Power Generation Using Externally Ionized, Cold, Supersonic Air as a Working Fluid", AIAA Journal, 44 (1),: Jan 2006, pp 119-127.

W. Beck, E. Stockman, S. Zaidi, and R. Miles, "Rayleigh Scattering Measurements for Obtaining Spatially-Resolved Absolute Gas Densities in Large-Scale Facilities," AIAA-2006-835, AIAA 44th Aerospace Sciences Meeting and Exhibit, Reno, Nevada, Jan. 9-12, 2006.

S. Macheret, "Physics of Magnetically Accelerated Nonequilibrium Surgace Discharges in High Speed Flow" AIAA-2006-1005, AIAA 44th Aerospace Sciences Meeting and Exhibit, Reno, Nevada, Jan. 9-12, 2006.

S. Zaidi, T. Smith, S. Macheret, and R. Miles, "Snowplow Surface Discharge in Magnetic Field for High Speed Boundary Layer Control," AIAA-2006-1006, AIAA 44th Aerospace Sciences Meeting and Exhibit, Reno, Nevada, Jan. 9-12, 2006.

Likhanskii, M. Shneider, S. Macheret and R. Miles, "Modeling of Interaction Between Weakly Ionized Near-Surface Plasmas and Gas Flow," AIAA-2006-1204, AIAA 44th Aerospace Sciences Meeting and Exhibit, Reno, Nevada, Jan. 9-12, 2006.

Z. Zhang, M. Shneider, S. Zaidi, and R. Miles, "Microwave Diagnostics of Small Volume Laser-Induced Plasma," AIAA-2006-1357, AIAA 44th Aerospace Sciences Meeting and Exhibit, Reno, Nevada, Jan. 9-12, 2006.

Z. Zhang, M. Shneider, and R. Miles, "Diagnostics by RADAR REMPI: Microwave Scattering from Laser-Induced Small Volume Plasmas", AIAA-2006-2971, 25th AIAA Aerodynamic Measurement Technology and Ground Testing Conference, San Francisco, CA, June 5-8, 2006

S.O. Macheret, M.N. Shneider, and R.B. Miles, "Modeling of Thermionic Devices with Plasmas Sustained by Repetitive Pulses", AIAA-2006-3385, 37th AIAA Plasmadynamics and Lasers Conference, San Francisco, CA, June 5-8, 2006

R.C. Murray, S.H. Zaidi, M.R. Carraro, L.M. Vasilyak, S.O. Macheret, M.N. Shneider, and R.B. Miles, "MHD Power Generation Using Externally Ionized, Cold, Supersonic Air as the Working Fluid," *AIAA Journal*, Vol. 44, No. 1, Jan 2006, pp. 119-127

S.O. Macheret, M.N. Shneider, and R.B. Miles, "Energy Efficiency of Plasma-Assisted Combustion in Ram/Scramjet Engines," *Paper AIAA 2005-5371*, 36th AIAA Plasmadynamics and Lasers Conference, Toronto, Ontario, Canada, 6-9 June 2005

M.N. Shneider and S.O. Macheret, "Modeling Plasma and MHD Effects in Hypersonic Propulsion Flowpath," *Paper AIAA 2005-5051*, 36th AIAA Plasmadynamics and Lasers Conference, Toronto, Ontario, Canada, 6-9 June 2005

S.O. Macheret, M.N. Shneider, R.C. Murray, and R.B. Miles, "Ionization in Strong Electric Fields and Dynamics of Nanosecond-Pulse Plasmas," *Paper AIAA-2005-0202*, 43rd AIAA Aerospace Sciences Meeting and Exhibit, Reno, Nevada, Jan. 10-13, 2005.

R.B. Miles, S.O. Macheret, M.N. Shneider, C. Steeves, R.C. Murray, T. Smith, and S.H. Zaidi, "Plasma-Enhanced Hypersonic Performance Enabled by MHD Power Extraction," *Paper AIAA-2005-0561* (Invited), 43rd AIAA Aerospace Sciences Meeting and Exhibit, Reno, Nevada, Jan. 10-13, 2005.

M.N. Shneider and S.O. Macheret, "Hypersonic Aerodynamic Control and Thrust Vectoring by Nonequilibrium Cold- Air MHD Devices," *Paper AIAA-2005-0979*, 43rd AIAA Aerospace Sciences Meeting and Exhibit, Reno, Nevada, Jan. 10-13, 2005

S.O. Macheret, M.N. Shneider, and R.B. Miles, "Scramjet Inlet Control by Off-Body Energy Addition: A Virtual Cowl," AIAA Journal (Log #J26772), (2004).

G.G. Chernyi, S.A. Losev, S.O. Macheret, and B.V. Potapkin, *Physical and Chemical Processes in Gas Dynamics, Vol. II: Physical and Chemical Kinetics and Thermodynamics*, AIAA, 2004.

S.O. Macheret, M.N. Shneider, and R.B. Miles, "Scramjet Inlet Control by Off-Body Energy Addition: a Virtual Cowl," *AIAA Journal*, Vol. 42, No. 11, November 2004, pp. 2294-2302.

M.N. Shneider, S.O. Macheret, and R.B. Miles, "Analysis of Magnetohydrodynamic Control of Scramjet Inlets," *AIAA Journal*, Vol. 42, No. 11, November 2004, pp. 2303-2310.

S.O. Macheret, M.N. Shneider, and R.B. Miles, "Magnetohydrodynamic and Electrohydrodynamic Control of Hypersonic Flows of Weakly Ionized Plasmas," *AIAA Journal*, Vol. 42, No. 7, July 2004, pp. 1378-1387.

S.O. Macheret, M.N. Shneider, and R.B. Miles, "Analysis of Magnetohydrodynamic Control of Scramjet Inlets," AIAA Journal (Log #J26773), (2004).

S.O. Macheret, M.N. Shneider, R.C. Murray, S.H. Zaidi, L.M. Vasilyak, and R.B. Miles, "RDHWT/MARIAH II MHD Modeling and Experiments Review," AIAA-2004-2485, 24th AIAA Aerodynamic Measurement Technology and Ground Testing Conference, Portland, Oregon, June 28-July 1, 2004.

X.G. Pan, M.N. Shneider, and R.B. Miles, "Coherent Rayleigh-Brillouin Scattering in Molecular Gases," Physical Review A, Vol. 69, March 2004, Article #033814.

S.H. Zaidi, M.N. Shneider and R.B. Miles, "Shock-Wave Mitigation Through Off-Body Pulsed Energy Deposition," AIAA Journal, Vol. 42, February 2004, pp. 326-331.

X. Pan, M. Shneider, S. Zaidi, and R. Miles, "Bulk Viscosity Measurements Using Coherent Ryaleigh-Brillouin Scattering," AIAA-2004-0017, 42nd AIAA Aerospace Sciences Meeting and Exhibit, Reno, Nevada, Jan. 5-8, 2004.

L. Qian, L. Vasilyak, S.H. Zaidi, S.O. Macheret, and R.B. Miles, "Ultra-Narrow Linewidth, 254nm Mercury Lamp, Pumped by Nanosecond Electrical Pulser," AIAA-2004-0020, 42nd AIAA Aerospace Sciences Meeting and Exhibit, Reno, Nevada, Jan. 5-8, 2004.

S. Zaidi, R. Murray, M. Carraro, L. Vasilyak and R. Miles, "Diagnostics of Short-Pulsed, Sustained Plasmas in a Cold Air MHD Channel," AIAA-2004-0708, 42nd AIAA Aerospace Sciences Meeting and Exhibit, Reno, Nevada, Jan. 5-8, 2004.

R.C. Murray, L.M. Vasilyak, M.R. Carraro, S.H. Zaidi, M.N. Shneider, S.O. Macheret, R.B. Miles, "Observation of MHD Effects with Nonequilibrium Ionization in Cold Supersonic Air Flows," AIAA-2004-1025, 42nd AIAA Aerospace Sciences Meeting and Exhibit, Reno, Nevada, Jan. 5-8, 2004.

S.O. Macheret, M.N. Shneider, and R.B. Miles, "MHD Power Generation in SCRAMJET Engines in Conjunction with Inlet Control," AIAA-2004-1197, 42nd AIAA Aerospace Sciences Meeting and Exhibit, Reno, Nevada, Jan. 5-8, 2004.

S. Macheret, M. Shneider, R. Miles, J. Silkey, and P. Smereczniak, "Optimum Performance of Electron Beam-Driven MHD Generators for SCRAMJET Inlet Control," AIAA-2003-3763, 34th AIAA Plasmadynamics & Lasers Conference, Orlando, FL, June 23-26, 2003.

M. Shneider, S. Macheret, S. Zaidi, I. Girgis, and R. Miles, "Steady and Unsteady Supersonic Flow Control with Energy Addition," AIAA-2003-3862, 34th AIAA Plasmadynamics & Lasers Conference, Orlando, FL, June 23-26, 2003.

R. Murray, S. Zaidi, J. Kline, M. Shneider, S. Macheret, and R. Miles, "Investigation of a Mach 3, Cold Air, MHD Channel," AIAA-2003-4282, 34th Plasmadynamics & Lasers Conference, Orlando, FL, June 23-26, 2003.